Supporting information

Ultrabroad Wavelength Absorption in High-temperature Solar Selective Absorber Coatings Enabled by High-entropy Nanoceramic AlTiZrHfNbN for High Performance Solar-thermal Conversion

Shuai-Sheng Zhao [a, b], Cheng-Yu He [a], Kai Chen [a, b], Bao-Hua Liu [a], Xiao-Li Qiu [c], Hui-Xia Guo [d], Gang Liu [a, b] and Xiang-Hu Gao [a, b, *]

[a] Research and Development Center for Eco-Chemistry and Eco-Materials, State Key Laboratory of Solid Lubrication, Lanzhou Institute of Chemical Physics, Chinese Academy of Sciences, Lanzhou, 730000, China

[b] Center of Materials Science and Optoelectronics Engineering, University of Chinese Academy of Sciences, Beijing, 100049, China

[c] College of Physics and Engineering, Chengdu Normal University, Chengdu, 611130, China

[d] Key Laboratory of Bioelectrochemistry & Environmental Analysis of Gansu Province, College of Chemistry & Chemical Engineering, Northwest Normal University, Lanzhou, 730070, China

[*] Corresponding author.

E-mail address: gaoxh@licp.cas.cn (Xiang-Hu Gao).

Experiment section

1.1 Preparation of the multilayer coating

The AlTiZrHfNbN-based SSACs were fabricated onto mechanically polished glass, SS, and Si wafer substrates utilizing a commercial reactive RF magnetron sputtering system. For the substrates, ultrasonic cleaning was conducted with acetone and ethanol. Before the deposition process, the vacuum chamber was pumped down to lower than 5.5×10^{-6} mTorr. High purity AlTiZrHfNb (99.99%, Φ76 mm × 4 mm) and Si (99.99%, Φ76 mm × 4 mm) deposition targets were employed to deposit the absorption layers and antireflection layer. The substrates were located in the center of the vacuum chamber based on a rotating sample holder. The distance between the target and the substrate holder was maintained at 15 cm. The metal volume fraction of the absorption layers was controlled by gas flow rate and deposition time. The complete fabrication process was carried out under an argon plasma sputtering environment at a working pressure of 28 mTorr. The detailed deposition parameters are summarized in Table S1.

Table S1 The deposition parameters of SS/AlTiZrHfNbN(HMVF)/AlTiZrHfNbN(LMVF)/SiO_2 SSACs.

Layer	Gas flow rate (sccm)			Deposition time (min)	Target power density (W/cm^2)	
	Ar	N_2	O_2		$Al_{0.4}Hf_{0.6}NbTaTiZr$	Si
HMVF	28	4		9	5.49	0
LMVF	28	6		12.5	5.49	0
SiO_2	28	0	8	130	0	3.31

1.2 Characterization of coatings

Thermal stability tests were conducted to characterize the phase, morphology, and optical properties of the as-deposited coatings and after annealing at the temperatures range of 200-700 °C for 10 h under a low vacuum pressure of 1.5×10^{-1} Pa utilizing a tubular furnace. In the wavelength range of 245-1000 nm, the optical constants for the as-deposited coatings were characterized by spectroscopic phase-modulated ellipsometry (HORIBA JOBIN YVON, France) with an incidence angle of 70°. The spectral reflectance was measured by a UV-vis-NIR spectrophotometer (Perkin-Elmer, Lambda 950) equipped with a 150 mm integrating sphere at a near-normal incidence angle, covering the 0.3-2.5 μm wavelength range. The MIR (the 2.5-25 μm wavelength range) reflectance spectra were characterized by a Bruker Tensor 27 FT-IR spectrometer. The spectrally averaged solar absorptance (α), emittance (*ε,* 82 °C), and thermal emittance (ε_T) were defined by equations (1), (2), and (3) as follows [1, 2]:

$$\alpha = \frac{\int_{0.3\mu m}^{2.5\mu m} [1 - R(\lambda,\ Ta)] G(\lambda) d\lambda}{\int_{0.3\mu m}^{2.5\mu m} G(\lambda) d\lambda} \quad \text{(S1)}$$

$$\varepsilon = \frac{\int_{2.5\mu m}^{25\mu m} [1 - R(\lambda,\ Ta, \theta)] P(\lambda, T) d\lambda}{\int_{2.5\mu m}^{25\mu m} P(\lambda, T) d\lambda} \quad \text{(S2)}$$

$$\varepsilon_T = \frac{\int_0^{+\infty} \varepsilon P(\lambda,T) d\lambda}{\sigma T^4}$$

(S3)

Here, *R(T, λ), G(λ),and P(λ, T)* represent the wavelength-dependent spectral reflectance, the solar radiation power, and the blackbody radiation at temperature *T*, respectively. The reflectance spectra of the primary coating and after annealing were measured at 82 °C. Accordingly, α and ε_T of the samples at the annealing temperatures were calculated by MATLAB software based on the reflectance spectra. Our previous work suggests that the simulation thermal emittance results are underestimated by 3-4%. [3]

The structural stability and solar-thermal conversion efficiency ($\eta_{solar\text{-}th}$) of SSACs are determined as the evaluation of the overall optical performance of the solar-thermal systems, which is defined as follows: [4]

$$\eta_{solar-th} = \frac{\alpha CI - \varepsilon_T \sigma T^4}{CI},$$

(S4)

where *I* is the total solar radiation in the solar spectrum (AM 1.5G), *C* is the sun concentration ratio (1-1000), and ε_T is the thermal emittance at working temperatures (*T*, 273-1300 K) of the coating, which are summarized in Table S2. In addition, σ is the Stephen-Boltzmann constant (5.6696×10^{-8} W/m^2).

Table S2 Thermal emittance of the samples after annealing at 600 °C and 700 °C at different working temperatures.

Work Temperature	As-deposited	Annealed at 600 °C	Annealed at 700 °C
82 °C	0.12	0.09	0.09
200 °C	0.22	0.15	0.14
300 °C	0.31	0.23	0.21
400 °C	0.39	0.30	0.26
500 °C	0.47	0.36	0.32
600 °C	0.52	0.42	0.36
700 °C	0.58	0.46	0.40

Three parameters: the atomic size difference (δ_r), the mixing enthalpy (ΔH_{mix}), and the mixing entropy (ΔS_{mix}) have been defined by Zhang et al. to characterize the collective behavior of the involved elements in the designed HEAN AlTiZrHfNbN absorption layers, which were calculated using the following equations:[5, 6]

$$\delta_r = 100\sqrt{\sum_{i=1}^{n} c_i\left(1 - r_i/\bar{r}\right)^2} \tag{S5}$$

$$\Delta H_{mix} = \sum_{i=1, i\neq j}^{n} \Omega_{ij} c_i c_j \tag{S6}$$

$$\Delta S_{mix} = -R\sum_{i=1}^{n} c_i \ln c_i \tag{S7}$$

$$\bar{r} = \sum_{i=1}^{n} c_i r_i \tag{S8}$$

where c_i, r_i, *and* R are the atomic percentage, atomic radius, and the gas constant of

the ith involved element, respectively. $\Omega_{ij} = 4\Delta H_{mix}^{AB}$, where ΔH_{mix}^{AB} is the mixing enthalpy of binary AB compounds.

In addition, two more parameters, the electronegativity difference, Δχ, and the valence electron concentration VEC, should be considered, which have been confirmed to be useful in characterizing the phase stability of high entropy nanoceramic. They are defined by: [7]

$$\Delta\chi = \sqrt{\sum_{i=1}^{n} c_i\left(\chi_i - \bar{\chi}\right)^2} \tag{S9}$$

$$VEC = \sum_{i=1}^{n} c_i (VEC)_i \tag{S10}$$

where χ_i and $(VEC)_i$ correspond to the Pauling electronegativity and valence electron concentration for the i_{th} element, respectively. All the required data can be found in Refs., and they are listed in Table S3. [8]

The theoretical crystal lattice parameter, a_{mix}, of the AlTiZrHfNbN absorption layers can also be estimated using the rule of mixtures approach: [9]

$$a_{mix} = \sum c_i a_i \tag{S11}$$

where ai is the lattice parameter of the element.

Table S3 Atomic radius (r), Pauling electronegativity (χ), valence electron concentration (VEC), and crystal lattice parameter (a) of the involved elements in the designed HEAN AlTiZrHfNbN absorption layers.

Element	r (Å)	χ	VEC	a (Å)

Al	1.43	1.61	3	4.05
Ti	1.46	1.54	4	2.95
Zr	1.60	1.33	4	3.23
Hf	1.58	1.30	4	3.20
Nb	1.44	1.60	5	3.30
N	0.75	3.04	5	3.86

The microstructure of the SS/AlTiZrHfNbN(HMVF)/AlTiZrHfNbN(LMVF)/SiO_2 SSACs was carried out by scanning electron microscopy (SEM, SU8200, Tokyo, Japan). The infrared (IR) camera (FLIR-E6) was employed to record the temperature changes and thermal distribution images. The X-ray diffraction (XRD) patterns were carried out by a Rigaku D/max 2400/PC multipurpose diffractometer (Rigaku Corporation, Tokyo, Japan) with X-ray Kα radiation (λ = 1.54 Å) operated at 40 kV and 200 mA. The crystal textures of the as-deposited coating were determined by the high-resolution transmission electron microscopy (HRTEM, Jeol, JSM-7100F). Atomic force microscopy was employed to characterize the topography of the AlTiZrHfNbN-based coatings (AFM, SPI 3800N/SPA400 Japan). Raman analyses were carried out with confocal micro-Raman spectroscopy (LabRAM HR Evolution, HORIBA) at room temperature.

1.3 Numerical Simulations

The commercial FDTD method (Lumerical software) was used for numerical simulation. The thicknesses of the substrate and individual layers originate from the

measured results based on the cross-section SEM images. A plane wave from +z towards the z-direction is selected as the incident light source. The boundary conditions along the x- and y-axis were selected as periodic boundaries, while those along the z-axis were perfectly matched layers (PML). To improve the simulation accuracy, the mesh sizes were set to 1 nm.

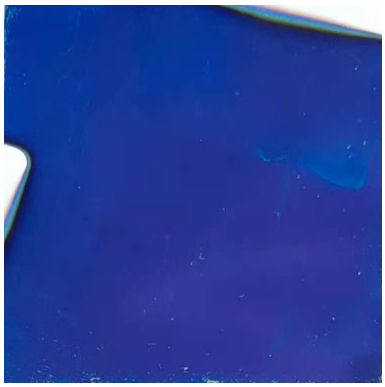

Fig. S1 Photograph of the as-deposited SS/AlTiZrHfNbN(HMVF)/AlTiZrHfNbN(LMVF)/SiO_2 SSACs

Table S4 The α values of single layer AlTiZrHfNbN coating with different N_2 gas flow.

N_2 gas flow rate	2 sccm	4 sccm	6 sccm	8 sccm
Absorptance	0.73	0.75	0.79	0.70

Table S5 Absorptance (α), emittance (ε), and spectral selectivity (α/ε) of the layer-added coatings.

Coating	α	ε	α/ε
SS	0.27	0.07	3.86
SS/HMVF	0.77	0.12	6.46
SS/HMVF/LMVF	0.83	0.11	7.36
SS/HMVF/LMVF/Al_2O_3	0.95	0.12	7.32

Table S6 Comparison of absorptance and wavelength of our as-deposited SSAC and recently reported SSACs.

Composites	α	λ	References
CL-GPR array	0.94	400-750	10
W-Ni-Al_2O_3 Cermet-Based	0.95	300-900	11
WTi-Al_2O_3 cermet-based	0.93	300-1000	12
SiO_2/9 vol% β-$FeSi_2$+SiO_2 composite/67 vol% β-$FeSi_2$+SiO_2 composite/SiO_2 barrier/Mo	0.96	300-1250	13
$AuAl_2$:AlN Nanoparticle Composites	0.97	300-1300	14
TSS-LAO	0.95	300-1350	15
Al/MoNbHfZrTiN/ MoNbHfZrTiON/SiO_2	0.935	300-1500	16
W/SiO_2	0.94	435-1520	17
Au/Al_2O_3/Au nanorods	0.95	900-1600	18
Co_3O_4 nanoparticles	0.892	300-1750	19
MgF_2/W	0.95	400-1800	20
Fe-SiO_2	0.90	400-2000	21
W/SiO_2/W	0.95	300-2000	22
W-SiO_2 Ceramic Composite.	0.95	300-2500	23
Au/Ge	0.90	200-2900	24

AlTiZrHfNbN-based	0.95	300-3220	This work

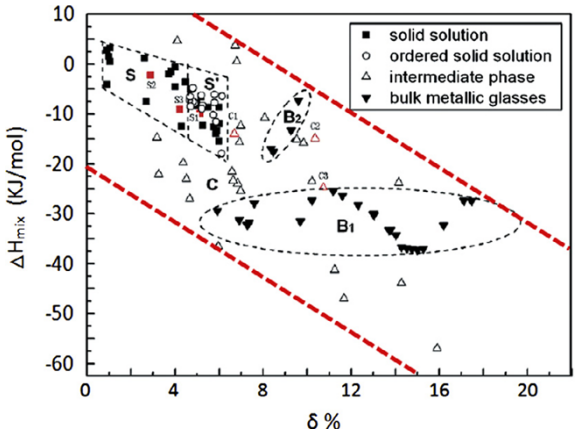

Fig. S2 A phase formation map based on the enthalpy of mixing ΔH_{mix} and the atomic size difference δ. For the formation of random solid solution, $15 < \Delta H_{mix} < 5$ kJ/mol, $\delta < 5\%$. The transition region is composed of an ordered solution and disordered solution mixture, where $20 < \Delta H_{mix} < 0$ kJ/mol, $5\% < \delta < 6.6\%$. Zones B1 and B2 are glass forming zones, and the rest are intermetallic compounds. [25]

Table S7 The crystal structures and lattice constants of individual nitrides in HfNbTaTiZrN.

Nitride	TiN	ZrN	HfN	NbN
Crystal structure Crystal spacing (nm)	fcc	fcc	fcc	fcc
(111)	2.54	2.64	2.61	2.53
(200)	2.20	2.29	2.26	2.19
(220)	1.56	1.62	1.60	1.55

Table S8 The crystal structures and lattice constants of AlN.

Nitride Crystal structure Crystal spacing (nm)	(100)	(110)	(200)
AlN (hcp)	3.717	6.451	7.463

Table S9 Elemental contents in the surface of the as-deposited SS/AlTiZrHfNbN(HMVF)/AlTiZrHfNbN(LMVF)/SiO_2 SSACs.

Element	Mass fraction (%)	Atomic fraction (%)
Al	1.47	2.71
Ti	5.69	5.92
Zr	14.31	7.81
Hf	39.31	10.97
Nb	15.98	8.57
Si	7.35	13.03
N	3.38	12.03
O	12.51	38.95

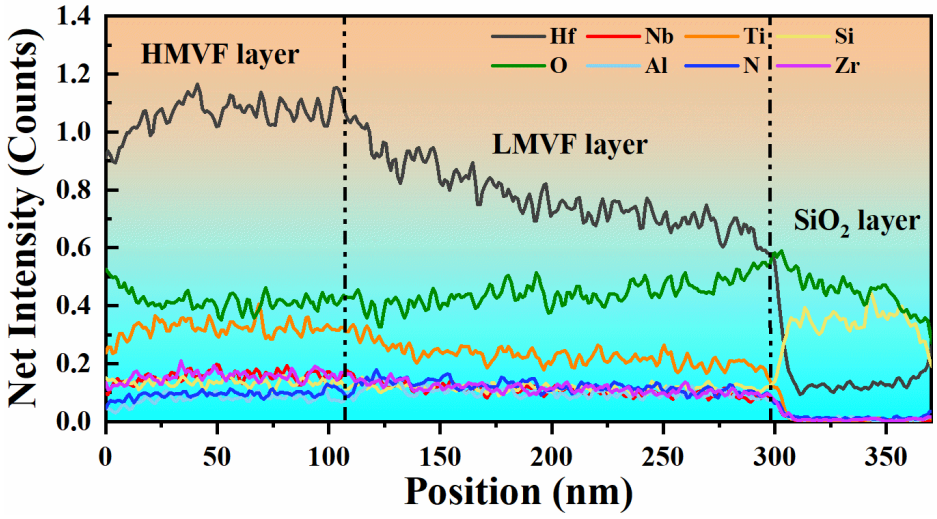

Fig S3 Line scan data along with the cross-section of the absorber coating.

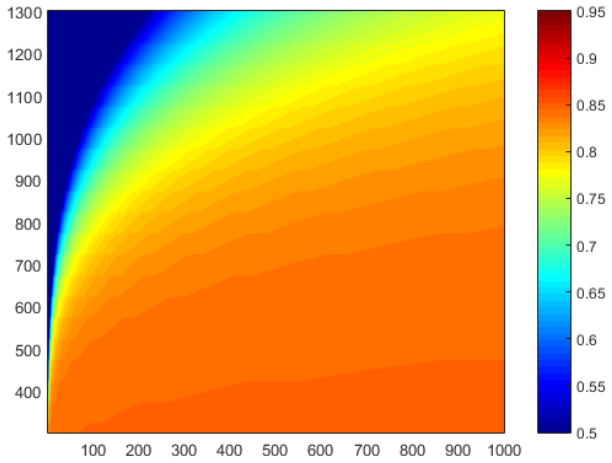

Fig. S4 Solar-thermal conversion efficiency of the sample annealed at 700 °C at different concentration ratios and different working temperatures.

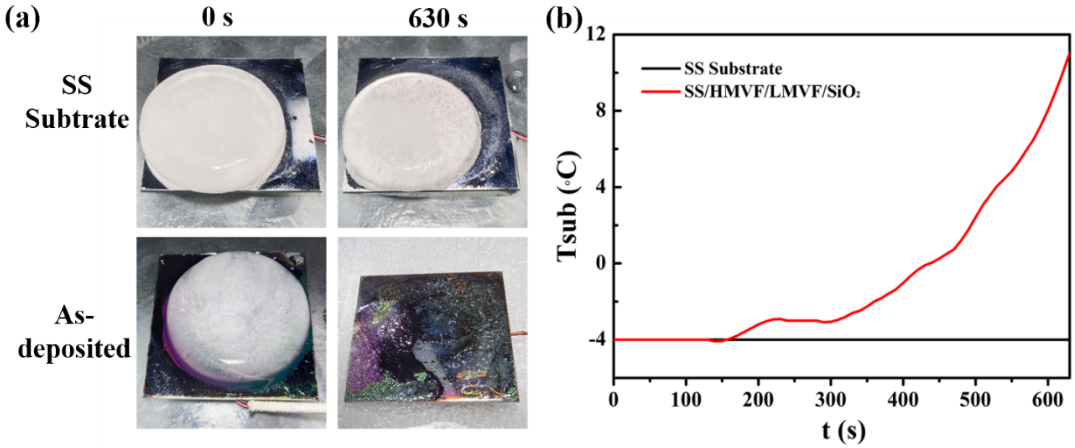

Fig. S5 (a) Melting of ice on the SS substrate and as-deposited coating, shown at 0 and 630 s after initial exposure to sunlight (C=1). (b) The substrate temperature variations of the respective groups.

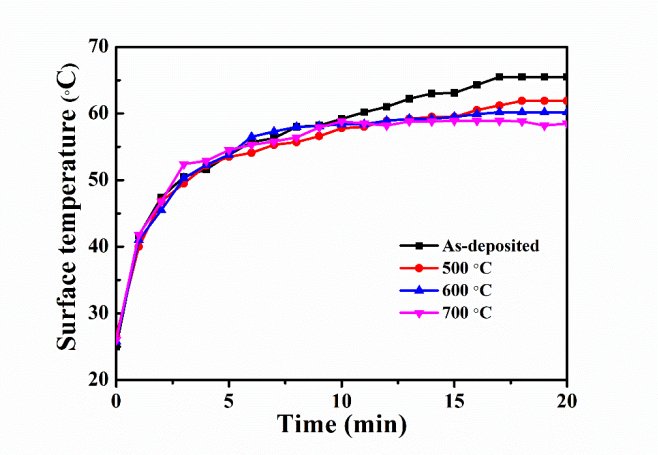

Fig. S6 Surface temperature variation acquired from coatings before and after annealing at 500 °C, 600 °C, and 700 °C under 1 sun irradiation for various times.

Table S10 Electronegativity difference, $\Delta\chi$, valence electron concentration, VEC, enthalpy of mixing ΔH_{mix}, entropy of mixing, ΔS_{mix}, atomic size difference, δr, and crystal lattice parameter, a, of the involved binary compound and the designed HEAN AlTiZrHfNbN absorption layers.

Compound	$\Delta\chi$	VEC	ΔH_{mix} (kJ/mol)	ΔS_{mix} (J/K/mol)	δ_r (%)	a_{mix} (Å)	Phases
AlN	0.72	4	-92	5.76	31.19	3.96	hcp
TiN	0.75	4.5	-190	5.76	32.28	3.41	fcc
ZrN	0.85	4.5	-233	5.76	36.17	3.55	fcc
HfN	0.87	4.5	-218	5.76	35.62	3.53	fcc
NbN	0.72	5	-174	5.76	31.51	3.58	fcc
AlTiZrHfNbN	0.36	4.37	-147.06	14.22	25.55	3.41	fcc

References

1 M. K. Gunde, J. K. Logar and Z. C. Orel, *Thin Solid Films*, 1996, **277**, 185-191.

2 Y. Mastai, S. Polarz and M. Antonietti, *Adv. Funct. Mater.*, 2002, **12**, 197-202.

3 C. -Y. He, X. -H. Gao, D. -M. Yu, S. -S. Zhao, H, -X. Guo and G. Liu, *J. Mater. Chem. A*, 2021, **9**, 21270.

4 Y. Li, C. Lin, Z. Wu, Z. Chen, C. Chi, F. Cao, D. Mei, H. Yan, C. Y. Tso, C. Y. H.Chao and B.Huang, *Adv. Mater.*, 2020, **10**, 202005074.

5 Y. Zhang, X. Yang and P. K. Liaw, *JOM*., 2012, **64**, 830-838.

6 X. Yang and Y. Zhang, *Mater. Chem. Phys.*, 2012, **132**, 233-238.

7 O. N. Senkov, S. V. Senkova and C. Woodward, *Acta Mater.*, 2014, **68**, 214-228.

8 S. Guo and C.T. Liu, *Prog. Nat. Sci.*, 2011, **21**, 433-446.

9 O. N. Senkov, G. B. Wilks, D. B. Miracle, C. P. Chuang and P., K. Liaw, *Intermetallics*, 2010, **18**, 1758-1765.

10 M. G. Nielsen, A. Pors, O. Albrektsen and S. I. Bozhevolnyi, *Opt. Express*, 2012, **20**, 13311-13319.

11 F. Cao, D. Kraemer, T. Sun, Y. Lan, G. Chen and Z. Ren, *Adv. Energy Mater.*, 2015, **5**, 1401042.

12 X. Wang, J. Gao, H. Hu, H. Zhang, L. Liang, K. Javaid, F. Zhuge, H. Cao and L. Wang, *Nano Energy*, 2017, **37**, 232-241.

13 Y. Okuhara, D. Yokoe, T. Kato, S. Suda, M. Takata, K. Noritake and A. Sato, *Sol. Energy Mater. Sol. Cells*, 2017, **161**, 240-246.

14 M. Bilokur, A. Gentle, M. D. Arnold, M. B. Cortie and G. B. Smith, *Sol. RRL*,

2017, **1**, 1700092.

15 F. Cao, L. Tang, Y. Li, A. P. Litvinchuk, J. Bao and Z. Ren, *Sol. Energy Mater. Sol. Cells*, 2017, **160**,12-17.

16 H. -X. Guo, C. -Y. He, X. -L. Qiu, Y. -Q. Shen, G. Liu and X. -H. Gao, *Sol. Energy Mater. Sol. Cells*, 2020, **209**, 110444.

17 D. Wu, Y. Liu, Z. Xu, Z. Yu, L. Yu, L. Chen, C. Liu, R. Li, R. Ma, J. Zhang and H. Ye, *Sol. RRL*, 2017, **1**, 1700049.

18 X. Chen, H. Gong, S. Dai, D. Zhao, Y. Yang, Q. Li and M. Qiu, *Opt. Lett.*, 2013, **38**, 2247-2249.

19 T. K. Kim, B. VanSaders, J. Moon, T. Kim, C. -H. Liu, J. Khamwannah, D. Chun, D. Choi, A. Kargar, R. Chen, Z. Liu and S. Jin, *Nano Energy*, 2015, **11**, 247-259.

20 H. Wang, V. Prasad Sivan, A. Mitchell, G. Rosengarten, P. Phelan and L. Wang, *Sol. Energy Mater. Sol. Cells,* 2015, **137**, 235-242.

21 D. Wu, C. Liu, Y. Liu, L. Yu, Z. Yu, L. Chen, R. Ma and H. Ye, *Opt. Lett.*, 2017, **42**, 450-453.

22 S. Han, J. -H. Shin, P. -H. Jung, H. Lee and B. J. Lee, *Adv. Opt. Mater.,* 2016, **4**, 1265-1273.

23 J. Yang, H. Shen, Z. Yang, Y. Zuo, Y. Zong, X. Huo and Y. Li, *Sol. RRL*, 2020, **4**, 2000336.

24 Q. Liang, W. Yu, W. Zhao, T. Wang, J. Zhao, H. Zhang and S. Tao, *Opt. Mater. Express,* 2013, **3**, 1187-1196.

25 Y. Zhang, T. Zuo, Z. Tang, M. C. Gao, K. A. Dahmen, P. K. Liaw and Z. P. Lu,

Prog. Mater. Sci., 2014, **61**, 1-93.